Materials Today Physics 45 (2024) 101469

Contents lists available at ScienceDirect

Materials Today Physics

journal homepage: www.journals.elsevier.com/materials-today-physics

Ultrahigh thermal conductance of the point contact between amorphous nanowires

Renzong Wang [a], Yucheng Xiong [a,*], Juekuan Yang [b], Zhichun Liu [c], Shouhang Li [a], Ge Chen [a], Ke Chen [d], Xiangjun Liu [a]

[a] Institute of Micro/Nano Electromechanical System, College of Mechanical Engineering, Donghua University, Shanghai, 201620, PR China
[b] School of Mechanical Engineering, Jiangsu Key Laboratory for Design and Manufacture of Micro-Nano Biomedical Instruments, Southeast University, Nanjing, 210096, PR China
[c] School of Energy and Power Engineering, Huazhong University of Science and Technology, Wuhan, 430074, PR China
[d] Center for the Physics of Low-Dimensional Materials, School of Physics and Electronics, School of Future Technology, Henan University, Kaifeng, 475004, PR China

ARTICLE INFO

Keywords:
Interfacial thermal conductance
Point contact
Amorphous nanowires
Heat conduction
Phonon transport

ABSTRACT

Amorphous interfaces/contacts are ubiquitous in numerous micro/nanoelectronic devices and functional composite materials. Traditionally, the thermal resistance of interfaces/contacts was believed to be the primary impediment to heat transport. However, in this study, through measuring thermal resistance between crystalline-amorphous core-shell Ge nanowires, we unveil an ultrahigh thermal conductance across the point contact between the amorphous shell of Ge nanowires with a room-temperature value of 892 MW/m^2-K. This value surpasses the typical values observed in point contacts between crystalline nanowires/nanoribbons by one to three orders of magnitude and even exceeds that of epitaxial interfaces between well-lattice-matched materials. Molecular and lattice dynamic simulations further reveal that the observed ultrahigh thermal conductance is attributed to the broadened vibrational bandwidths within the amorphous contact, which facilitates the redistribution of phonon energy into a state conductive to more effective interfacial energy transmission, leading to an enhanced overlap of phonon modes and, consequently, a heightened thermal conductance.

1. Introduction

Nanoscale interfaces/contacts between amorphous semiconductors are ubiquitous in numerous micro/nanoelectronic and optoelectronic devices, including transistors [1,2], phase-change memory [3,4], memristors [5], and photosensors [6,7]. The substantial thermal resistance at these nanoscale amorphous interfaces/contacts constitutes a critical impediment to heat transport, especially as the characteristic dimensions approach the mean free path of energy carriers. This presents a formidable heat dissipation challenge to modern electronics [8–10]. For example, thin amorphous dielectric layers, such as SiO_2 [11], HfO_2 [12], Al_2O_3 [13], and SiN_x [14], commonly function as gate insulators in metal-oxide-semiconductor field-effect transistors. As the thickness of these amorphous layers diminishes below 2 nm [15], the thermal resistance at the interface/contact approaches or even surpasses that of the constituent materials. As such, a fundamental understanding of thermal transport through nanoscale amorphous interface/contact is needed for the advancement of electronic device design.

The incorporation of an amorphous phase into a crystalline system has been observed to impede thermal transport [16–18]; however, whether this phenomenon holds true at the interface/contact remains debated. For example, through examining the modal transmission and reflection processes across the interface using mode-resolved atomistic Green's functions, Yang *et al.* reported that the thermal conductance was reduced by a factor of 75% from 1.11 GW/m^2-K for crystalline Si interface to 0.28 GW/m^2-K for amorphous interface [16]. In addition, introducing an amorphous phase at Si/Al and AlN/GaN interfaces notably reduced interfacial thermal conductance, with tunability influenced by the strength of interfacial bonding [17,18]. Contrary to prevailing observations, recent computational investigations have demonstrated that amorphous interfaces can exhibit substantially higher thermal conductance in comparison to their crystalline counterparts. Notably, non-equilibrium molecular dynamic (NEMD) simulations by Giri *et al.* disclosed a conductance of 1.92 GW/m^2-K for the amorphous Si/Ge interface, approximately sixfold higher than its crystalline counterpart [19]. A similar heightened conductance across the

* Corresponding author.
E-mail address: ycxiong@dhu.edu.cn (Y. Xiong).

https://doi.org/10.1016/j.mtphys.2024.101469
Received 14 March 2024; Received in revised form 6 May 2024; Accepted 22 May 2024
Available online 23 May 2024

amorphous Si/Ge interface was predicted by Goridz *et al.* through MD simulation [20]. This discrepancy in thermal conductance is explained by the different heat-carrying vibrations, with non-propagating modes (diffusons) dominating in amorphous interfaces, while propagating modes (propagons) predominantly contribute to thermal transport in crystalline counterparts [19,20].

On the experimental side, despite the robust experimental techniques for thermal transport across crystalline interfaces, the minimal temperature drop across amorphous interfaces, resulting from the inherently low thermal conductivity of amorphous materials, poses significant challenges in accurately quantifying interfacial thermal conductance. To overcome these challenges, Giri *et at.* fabricated amorphous superlattice structures and employed a thermal resistor model to determine the conductance across an individual interface. They reported an ultrahigh thermal conductance of 909 MW/m^2-K across the amorphous SiOC:H/SiC:H interface [21]. However, the preparation processes for superlattice samples are quite complex. In addition, the thermal resistor model is based on a physical picture of diffusive transport; while recent experimental observations of size-dependent thermal conductivity suggested quasi-ballistic transport in amorphous solids [22,23], making the applicability of the thermal resistor model questionable.

To address the aforementioned issues, this study employs crystalline-amorphous core-shell Ge nanowires to construct the amorphous point contact. The high thermal conductivity of the crystalline Ge core facilitates a measurable temperature drop across the contact between the amorphous shell of the nanowires. Systematic thermal measurements of the contact sample and the corresponding single nanowires are conducted using a well-established thermal bridge method. The results reveal an ultrahigh thermal conductance for the amorphous point contact. The underlying mechanisms are further analyzed through NEMD simulations.

2. Material and methods

2.1. Materials

Crystalline-amorphous core-shell Ge nanowires were synthesized using the chemical vapor deposition method, as thoroughly described in previous work [24]. The crystallographic structure and chemical composition of the obtained nanowires were characterized by high-resolution transmission electron microscopy (HRTEM) and HRTEM energy-dispersive X-ray spectroscopy (HRTEM-EDS), respectively. As shown in Fig. 1, the synthesized nanowires exhibit a crystalline core and an amorphous shell with thickness comparable to the crystalline core.

2.2. Thermal measurement

Thermal resistance measurements for the nanowire were conducted employing a well-established thermal bridge method within a high-vacuum cryostat system ($<10^{-6}$ mbar), covering a temperature range from 20 to 300 K [25,26]. The micro-device employed in this investigation consists of two suspended silicon nitride membranes featuring integrated platinum coils, acting as a heater and thermometer for thermal measurement. A Wheatstone bridge circuit was implemented by introducing a blank device on the sensing side to improve measurement sensitivity [26].

To validate the assumed constant contact thermal resistance between the nanowire and the two membranes as well as to measure the intrinsic thermal conductivity of the Ge nanowire, a single nanowire was measured at three different suspended lengths from 20 to 300 K. At each temperature point, the measured thermal resistance was fitted against

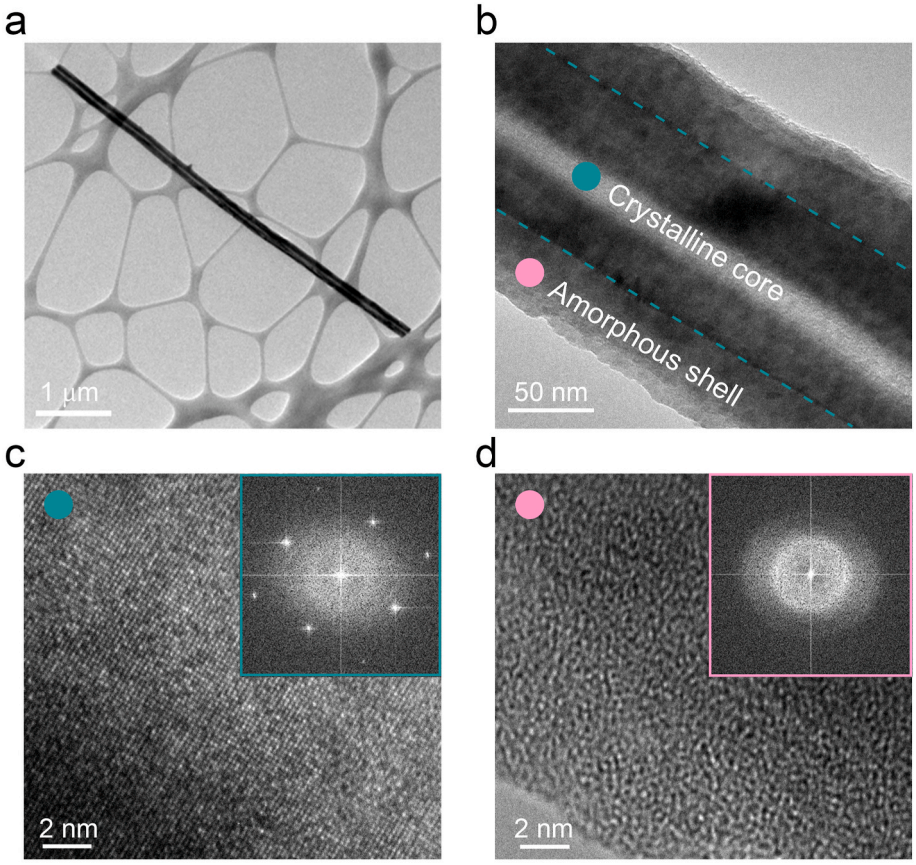

Fig. 1. (a) TEM and (b) HRTEM images of the crystalline-amorphous core-shell Ge nanowire. The dash lines in (b) indicate the core-shell boundaries. HRTEM images on (c) the core and (d) the shell of Ge nanowire. The insets in (c) and (d) show the corresponding selected area electron diffraction pattern.

the suspended length. The linear relationship observed between the measured thermal resistance and the suspended length verified the assumption of constant contact thermal resistance, with the slope and y-axis intercept of the fitted line representing the thermal resistance per unit length and the contact thermal resistance with the two membranes, respectively. Combining this information with geometric details obtained from scanning electron microscopy (SEM) characterization enabled the determination of the nanowire's intrinsic thermal conductivity.

2.3. NEMD simulations

NEMD simulations were performed utilizing the large-scale atomic/molecular massively parallel simulator (LAMMPS) package [27]. The amorphous interface state was achieved by subjecting the material to a heating process from 300 to 4000 K, maintained for 1 ns, followed by rapid quenching to room temperature at a rate of 1.5×10^{15} K/s, with the remaining atoms held fixed [28]. The interaction between the atoms at the contact was described by the Lennard-Jones potential. The associated parameters were calculated based on the universal force field and interactions among the remaining atoms in the system were modeled using the Tersoff potential [29,30]. Lennard-Jones potentials were subjected to a cutoff distance of 10 Å and a timestep of 0.5 fs was chosen. Periodic boundary conditions were applied in the in-plane (x–y) direction, while free boundary conditions were imposed in the out-of-plane (z) direction. More details are given in the Supplementary Material.

3. Results and discussion

Fig. 1 depicts HRTEM images of the measured sample. The nanowire exhibits a uniform diameter with a core diameter of approximately 94 nm and a shell thickness of about 42 nm (Fig. 1a and b). Selected area electron diffraction (SAED) patterns acquired at the nanowire center confirm the fine single-crystalline structure of the nanowire core (Fig. 1c). In contrast, SAED patterns obtained at the nanowire surface reveal diffuse rings typical for an amorphous structure (Fig. 1d). The HRTEM-EDS analysis indicates that the nanowire primarily comprises Ge with a tiny O peak (Fig. S1), potentially originating from the native oxide surface layer. The SAED and EDS results collectively confirm that the nanowires are crystalline Ge nanowires enveloped by amorphous GeO_x shells.

To avoid nanowire-to-nanowire variation during the extraction of point contact thermal conductance, a uniform crystalline-amorphous core-shell Ge nanowire, spanning tens of microns in length, was cut into two segments using a precision-controlled sharp tip mounted on an in-house built micromanipulator. These segments were then transferred to bridge the two suspended membranes, forming a cross-contact sample, as shown in Fig. 2a for sample S1. The suspended length of the contact sample is 7.69 μm with a diameter of 178 nm. A core-shell structure was discernible under SEM, as depicted in the inset of Fig. 2a. The measured thermal resistance of the contact sample (R_{tot_C}) can be expressed as

$$R_{tot\_C} = R_{CM} + R_{nw\_C} + R_C \quad (1)$$

where R_{nw_C}, R_C, and R_{CM} represent the thermal resistance of the 7.69 μm-long nanowire, the contact thermal resistance between nanowires, and the contact thermal resistance between the nanowire and the two membranes, respectively. After thermal measurement on the cross-contact sample, one segment was removed, while the other was realigned and adjusted to approximate the suspended length of the cross-contact sample (Fig. 2b), with a suspended length measured as 7.59 μm. The thermal resistance of the single sample can be written as

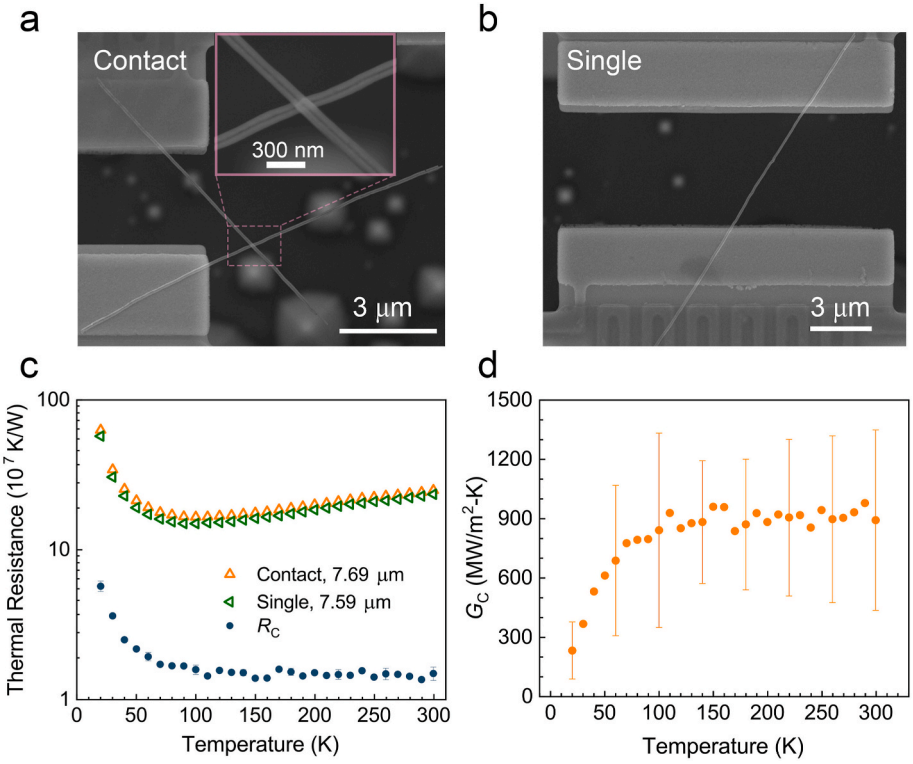

Fig. 2. SEM micrographs of (a) two crystalline-amorphous core-shell Ge nanowires with a point contact and (b) the corresponding single continuous nanowire on a suspended device for thermal measurement (sample S1). The suspended length is 7.69 μm and 7.59 μm for the contact and the single sample, respectively. The inset in (a) shows the zoom-in view of the point contact. (c) Measured thermal resistance of the point-contact sample and the single nanowire and the extracted thermal resistance of the point contact, R_C. (d) Contact thermal conductance (G_C) of the point contact between the amorphous shell of Ge nanowires. The diameter of the nanowire is 178 nm and the contact area between nanowires is calculated to be 74.9 nm^2.

$$R_{tot\_S} = R_{CM} + R_{nw\_S} \quad (2)$$

where R_{nw_S} denotes the thermal resistance of the 7.59 μm-long nanowire. Assuming a constant R_{CM} for both measurements and neglecting the difference in suspended length, R_C was deduced by comparing the measured thermal resistance as $R_C = R_{tot\_C} - R_{tot\_S}$. To facilitate the assumption of a constant R_{CM}, the contact length between the nanowire and the membranes exceeds 4 μm to ensure thermal equilibrium with the membranes. Note that this contact length required for full thermalization approximates 1 μm according to the fin heat transfer model [31]. Thus, the R_{CM} could be regarded as a constant. Further measurements on the same nanowire at three different suspended lengths were performed to validate the assumption of constant R_{CM}.

Fig. 2c shows that the measured thermal resistance of the contact sample slightly exceeds that of the single nanowire and shares a consistent temperature trend. The thermal resistance experiences a rapid decrease initially, reaching a minimum value at approximately 90 K, followed by a gradual increase up to 300 K. By comparing the measured resistances of the two samples, the contact thermal resistance of the point contact between nanowires (R_C) is extracted and plotted by the blue circle in Fig. 2c. R_C exhibits a distinct temperature dependence relative to the nanowire sample, monotonically decreasing at low temperatures until ~90 K, then plateauing at approximately 1.4×10^7 K/W at 300 K. It is noteworthy that the relative uncertainty of the measured thermal resistance is 4% above 100 K and less than 2% below 100 K. The extracted R_C carries an uncertainty of less than 58% above 100 K and 61% below 100 K, according to the standard error propagation [32]. The detailed uncertainty analysis is given in the Supplementary Material.

To further understand the results of point contact resistance, we normalize R_C with the contact area between two nanowires. Fig. S2 shows the cross-section of Ge nanowires of different sizes, which is prepared through sharp probe cutting followed by SEM characterization. The core-shell Ge nanowires studied in this work exhibit a circular cross-section. Three widely used theoretical models—the JKR model [33], the DMT model [34], and the Maugis model [35]—are considered for determining the contact area between a sphere and a plane. The transition across these models is described by a dimensionless transition parameter, denoted as μ. Upon integrating the material properties of the nanowire, the value of μ is calculated to be 0.28, thereby indicating that the Maugis model applies. More details are given in the Supplementary Material. The contact area between the core-shell nanowires with a diameter of 178 nm is calculated to be 74.9 nm^2. This value slightly exceeds the 57.8 nm^2 observed between multi-wall carbon nanotubes (MWCNTs) with a diameter of 68 nm, due to the higher Young's modulus of Ge compared to WMCNT [36].

Fig. 2d plots the contact thermal conductance per unit area (G_C) as a function of temperature. G_C follows the typical temperature trend for interfacial thermal conductance, escalating rapidly at low temperatures and reaching a plateau beyond 90 K. Measurements on a different sample (sample S2) following the same approach yielded consistent results, as shown in Fig. S3. It is noteworthy that if phonons from the crystalline core can ballistically propagate through the thin amorphous interlayer, the transmission ratio of these phonons will tend towards unity given the same materials on both sides of the amorphous interlayer [37], thus resulting in an enhanced G_C. Prior wave packet simulations on Si/amorphous SiO_2/Si sandwiched structures have suggested that low-frequency phonons possess the ability to ballistically penetrate through a 10 nm amorphous SiO_2 layer [38]. Recent measurements on double Si nanoribbons with an amorphous SiO_2 layer sandwiched in-between have further confirmed this phenomenon, demonstrating ballistic penetration through amorphous SiO_2 up to 5 nm at room temperature [39]. Given that Ge exhibits a smaller phonon mean free path compared to Si due to its heavier atomic mass, it is reasonable to anticipate that the ballistic phonon penetration depth in amorphous GeO_x layer would be smaller than that observed in amorphous SiO_2 (typically in the range of 5–10 nm). Considering that the thickness of amorphous layer in our sample is tens of nanometers, it is concluded that the phonons from the crystalline core are unable to ballistically penetrate through the amorphous interlayer.

At room temperature, the value of G_C reaches 892 MW/m^2-K, markedly surpassing most reported G_C value in the literature for the crystalline vdW contacts, as illustrated by the open symbols in Fig. 3. Yang *et al.* measured contact thermal resistance between MWCNTs and reported a G_C on the order of 10^8 W/m^2-K at room temperature [36], as shown by blue open squares in Fig. 3. The G_C of the planar contact between crystalline copper phthalocyanine (CuPc) nanoribbons was reported to be on the order of 10^5 W/m^2-K (purple open stars) [40], owing to the rather weak vdW interaction and substantially reduced real contact area induced by nanoscale surface roughness. A similar ultralow G_C in the range of 10^5-3.5×10^6 W/m^2-K between a Bi_2Te_3 nanoplate and Pt electrodes was reported by Pettes et al. (black open triangles) [41]. Compared to these crystalline contacts, the obtained G_C for the point contact between amorphous nanowires is approximately one order of magnitude higher than that of the point contact between MWCNTs, and approximately three orders of magnitude higher than the planar contact between nanoribbons. The markedly low G_C of the planar contact is attributed to the limited intimate contact between two rough nanoribbons, which primarily occurs at a restricted number of protruding asperities [40]. For example, Persson and Scarraggi showed that the real-to-nominal contact area ratio remains approximately 0.06 under zero external load for planar surfaces with a root-mean-square roughness of 0.6 nm and an adhesion energy of 0.1 J/m^2 (value typical for vdW interfaces) [42,43]. In contrast, the point contact between nanowires involves two cylindrical structures with nanometer-scale radii of curvature coming into contact, which could render an enlarged effective contact area relative to the planar contact. Furthermore, the lower elastic modulus of the amorphous layer compared to its crystalline counterpart facilitates elastic deformation upon contact, thereby further enlarging the contact area.

Fig. 3 further compares the measured G_C for the amorphous point contact with those reported for crystalline/amorphous interfaces, as marked by half-filled symbols. Interfacial thermal transport across crystalline interfaces has been extensively investigated using well-established theoretical models and robust experimental techniques. Typical thermal conductance for a crystalline interface falls within the ranges from 20 to 300 MW/m^2-K, depending on factors such as interface quality, bonding strength, and phonon properties of constituent materials [44,45]. The upper limit for phonon-dominant interface is represented by the thermal conductance of epitaxial interfaces between well

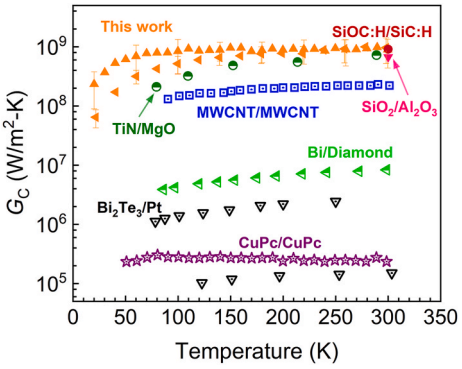

Fig. 3. Comparison of the G_C for the point contact between amorphous Ge nanowires with those reported for crystalline MWCNT/MWCNT point contact [36], crystalline CuPc/CuPc planar contact [40], crystalline Bi_2Te_3/Pt planar contact [41], crystalline TiN/MgO interface [46], crystalline Bi/diamond interface [45], amorphous SiOC:H/SiC:H interface [21], and amorphous SiO_2/Al_2O_3 interface [47]. Open symbols are data for crystalline point contacts, half-filled symbols are for crystalline interfaces, and filled symbols are for amorphous interfaces/contacts.

lattice-matched materials, such as TiN/MgO interface (olive half-filled circles) [46]; while the interfaces between highly dissimilar materials, such as Bi/diamond (green half-filled triangles) [45], stand as the lower limit. In comparison, interfacial conductance across the amorphous interfaces has received much less attention. Fong *et al.* reported a high thermal conductance of 670 MW/m^2-K between the amorphous SiO_2 and Al_2O_3 interface using steady-state Joule-heating and electrical thermometry (pink-filled triangle) [47]. This unusually high thermal conductance was explained by the broadened phonon modes between amorphous materials. Recently, Giri *et al.* demonstrated an ultrahigh conductance of 909 MW/m^2-K at amorphous SiOC:H/SiC:H interfaces using a time-domain thermoreflectance technique, attributing it to non-propagating modes in the amorphous interface (red filled circle) [21]. Compared with these studies, the measured G_C of the point contact between amorphous Ge nanowires slightly surpasses that of the crystalline TiN/MgO interface [46], and is approximately two orders of magnitude higher than of the crystalline Bi/diamond interface [45], but closely aligns with the G_C reported for the amorphous SiOC:H/SiC:H and SiO_2/Al_2O_3 interfaces [21,47].

To elucidate the underlying mechanisms for the observed ultrahigh G_C, NEMD simulations were performed on thermal transport through the amorphous and crystalline contact between Ge nanowires. The precise quantification of oxygen concentration within an amorphous GeO_x layer *via* TEM is challenging. Here we employed two extreme scenarios, Ge and GeO_2, to evaluate the effect of amorphous morphology on interfacial thermal transport. Fig. 4a illustrates the MD simulation system of two Ge nanowires forming a crystalline and amorphous contact, employing the Lennard-Jones potential to describe the vdW interaction between the atoms at the contact. Fig. 4b shows the temperature distributions along the Ge nanowires, from which the temperature drop (ΔT) across the contacts can be extracted. Specifically, ΔT is determined to be 32.5 K, 30.9 K, and 30.1 K for the crystalline Ge, amorphous Ge, and amorphous GeO_2 contacts, respectively, under identical heat source and heat sink temperatures. Consequently, the calculated G_C is 28.5 MW/m^2-K, 33.1 MW/m^2-K, and 39.6 MW/m^2-K for the crystalline Ge, amorphous Ge, and amorphous GeO_2 contacts, respectively. Although direct comparison of G_C between the NEMD simulations and experimental results is challenging, it suggests that the thermal conductance across the amorphous interface is indeed greater than that across the crystalline interface. To further investigate this observation, we turn to material-specific lattice dynamics calculations. Fig. 4c compares the phonon density states (PDOS) of crystalline Ge, amorphous Ge, and amorphous GeO_2, derived from recorded atomic velocity during NEMD simulations and using an autocorrelation technique [48]. In crystalline Ge, phonon energy concentrates within a narrow frequency range from 3 to 12 THz, with distinct peaks around 5 and 10 THz. In comparison, PDOS spectra for amorphous Ge are smoother, with dramatically lowered peaks that slightly shift toward lower frequencies, broadening the available phonon modes for heat transport. Importantly, the cutoff frequency for vibrational spectra increases to 15 THz. For amorphous GeO_2, PDOS spectra exhibit further smoother and broader profiles, with the cutoff frequency extending up to 25 THz. This broadened PDOS facilitates enhanced overlapping of phonon modes between amorphous contacts compared to crystalline counterparts, leading to effective thermal coupling and high thermal conductance [47,49].

Furthermore, recent studies on amorphous Si/Ge interfaces have suggested that the heat carriers across the interface differ significantly between the amorphous and crystalline interfaces [9,19–21]. For amorphous interfaces, dominant heat-carrying vibrations are non-propagating modes (diffusons), contrasting with the propagating modes (progagons) dominant in crystalline counterparts. The highly interacting vibration modes in the frequency region of 12–13 THz, which play an important role in perturbing the natural vibrations and affecting the thermal conductance of the crystalline Si/Ge interface, were observed to shift to a broader frequency region around 10–14 THz and contribute largely to thermal transport across the amorphous interface [20]. Transport between diffusions and locons may be enhanced by heat bath perturbation, while it is suppressed for the propagating modes existing in crystalline materials, thereby contributing to thermal transport at the amorphous interface. More rigorous theoretical calculations would be needed to further understand the unique vibrational modes at the amorphous interface.

To validate the assumed constant R_{CM} among different measurements as well as to determine intrinsic thermal conductivity, the same nanowire was measured at three different suspended lengths, as shown in Fig. 5a–c. Fig. 5d plots the measured thermal resistances for the three samples, with all three nanowires displaying a consistent temperature trend and higher thermal resistance values for larger suspended length samples. At each temperature point, the thermal resistance of the core-shell nanowire per unit length is derived through linear fitting of the

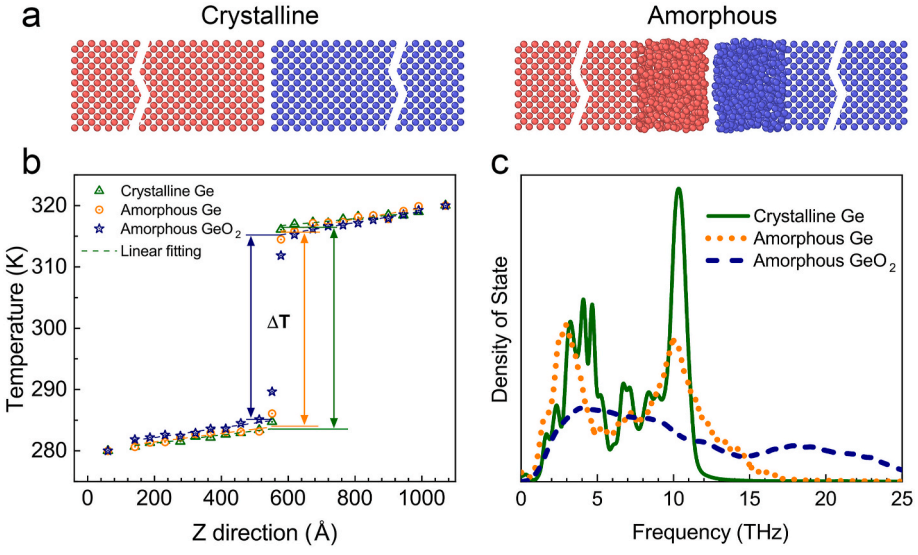

Fig. 4. (a) Schematics of the crystalline and amorphous contact between Ge nanowires in the NEMD simulations. (b) Temperature distributions along the nanowires for the crystalline Ge (olive open triangles), amorphous Ge (orange open circles), and amorphous GeO_2 (royal open stars) contacts. (c) Phonon density of states for the crystalline Ge (olive line), amorphous Ge (orange dot), and amorphous GeO_2 (royal dash). (For interpretation of the references to colour in this figure legend, the reader is referred to the Web version of this article.)

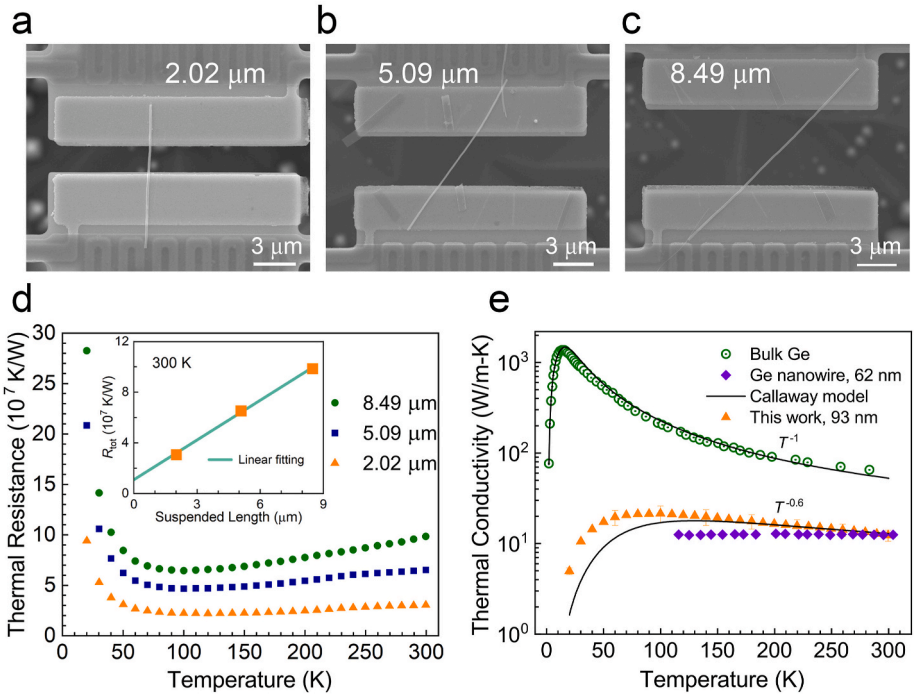

Fig. 5. Intrinsic thermal conductivity of Ge nanowire. SEM images showing the same Ge nanowire sample with a suspended length of (a) 2.02 μm, (b) 5.09 μm, and (c) 8.49 μm. (d) Corresponding measured thermal resistance as a function of temperature. The inset in (d) shows the linear fitting of thermal resistance against suspended length at 300 K. (e) Extracted intrinsic thermal conductivity of the crystalline Ge nanowire. Literature reports on bulk Ge [51] and Ge nanowire [52] are also plotted for comparison. The solid lines in (e) show the results of the modified Callaway model.

measured thermal resistance against the suspended length, as shown in the inset of Fig. 5d for 300 K. To account for the contribution of the amorphous shell, the thermal conductivity of amorphous Ge is estimated using a theoretical model [50]. More details are given in the Supplementary Material. The thermal resistance of the crystalline core is extracted based on the shell thickness using the parallel resistor model. Subsequently, the intrinsic thermal conductivity of crystalline Ge is determined with the core diameter. The relative uncertainty in thermal conductivity is less than 20% within the measured temperature range.

Fig. 5e compares the extracted intrinsic thermal conductivity of the crystalline Ge nanowire with literature reports [51,52]. For bulk Ge, thermal conductivity rapidly escalates at low temperatures, reaches a peak value of 1368.3 W/m-K at approximately 15 K, then decreases following the T^{-1} trend above 200 K, and saturates with a room-temperature value of 52.7 W/m-K. In comparison, the thermal conductivity of the Ge nanowire reaches a peak value of approximately 21.3 W/m-K at ~90 K, subsequently following a $T^{-0.6}$ trend above 200 K. The room-temperature thermal conductivity is 12.1 W/m-K, lower than the corresponding bulk value by a factor of ~4.4. Compared to the Ge nanowire with a smaller diameter of 62 nm, the measured thermal conductivity for the 94 nm nanowire exhibits a slightly larger value and a less flat temperature trend above 200 K [52].

To elucidate the reduction in thermal conductivity and the flatten temperature dependence, we employed the modified Callaway model to fit the thermal conductivity of bulk Ge and Ge nanowire [53].

$$\kappa = \kappa_L + 2\kappa_T \tag{3}$$

where

$$\kappa_i = \kappa_{i1} + \kappa_{i2} \tag{4}$$

The partial conductivities κ_{i1} and κ_{i2} ($i = T$ or L represents transverse or longitudinal acoustic phonons) are defined as:

$$\kappa_{i1} = \frac{k_B}{2\pi^2 v_B}\left(\frac{k_B T}{\hbar}\right)^3 \int_0^{\theta_i/T} \tau_C^i \frac{x^4 e^x}{(e^x-1)^2} dx \tag{5}$$

$$\kappa_{i2} = \frac{k_B}{2\pi^2 v_B}\left(\frac{k_B T}{\hbar}\right)^3 \frac{\left[\int_0^{\theta_i/T} \frac{\tau_C^i}{\tau_N^i} \frac{x^4 e^x}{(e^x-1)^2} dx\right]^2}{\int_0^{\theta_i/T} \frac{\tau_C^i}{\tau_N^i \tau_R^i} \frac{x^4 e^x}{(e^x-1)^2} dx} \tag{6}$$

where $x = \hbar\omega/k_B T$, ω is the phonon frequency, k_B is the Boltzmann constant, and $\hbar$ is the reduced Planck constant. v_B is the average phonon group velocity and taken as 3500 m/s [51] θ_i (i=T, L) is the Debye temperature and taken as 118 K and 333 K for the transverse and longitudinal branch, respectively [51]. τ_C^i, τ_R^i and τ_N^i (i=T, L) are the combined phonon relaxation time, the relaxation time for resistive processes, and the relaxation time for normal processes, respectively, which can be calculated by

$$\left(\tau_C^i\right)^{-1} = \left(\tau_R^i\right)^{-1} + \left(\tau_N^i\right)^{-1} \tag{7}$$

$$\left(\tau_R^i\right)^{-1} = \frac{v_B}{D} + A\omega^4 + B_{iU}\omega^2 T e^{-C_i/T} \tag{8}$$

$$\left(\tau_N^T\right)^{-1} = B_T \omega T^4 \tag{9}$$

$$\left(\tau_N^L\right)^{-1} = B_L \omega^2 T^3 \tag{10}$$

where D is the characteristic size. A, B_i, and B_{iU} (i=T, L) are fitting parameters. The three terms on the right side of Eq. (8) represent the phonon boundary scattering, point-defect scattering, and phonon-phonon Umklapp scattering, respectively. The parameters A, B_i and B_{iU} (i=T, L) were determined by fitting the measured thermal conductivity of bulk Ge reported in the literature [51], as shown by the solid line in Fig. 5e. The fitting parameters are list in Table 1. For Ge nanowire, all parameters were maintained at the same values as those for bulk Ge, with the exception that D was represented by the nanowire diameter, i.e., 94 nm. This value is over five orders of magnitudes lower than the corresponding value for bulk Ge, indicating a significantly enhanced phonon boundary scattering in the nanowire sample. As

Table 1
Fitting parameters for thermal conductivity of Ge nanowire in this work and bulk Ge in the literature [51].

	D (nm)	A (10^{-44} s^3)	B_T (10^{-13} K^{-4})	B_L (10^{-21} s/K^3)	B_{TU} (10^{-19}s)	B_{LU} (10^{-19}s)	C_T (K)	C_L (K)
Bulk Ge	3.8×10^6	1.78	2	2	1	5	55	180
Ge nanowire	94	1.78	2	2	1	5	55	180

depicted in Fig. 5e, the thermal conductivity value and its temperature trend for the Ge nanowire can be fitted quite well using the parameter in Table 1. Therefore, the observed reduction in thermal conductivity and the flattened temperature dependence compared to bulk Ge can be attributed to the enhanced phonon boundary scattering at the nanowire surface.

4. Conclusions

In summary, this study reports an ultrahigh thermal conductance of the amorphous point contact by measuring the contact thermal resistance between core-shell crystalline-amorphous Ge nanowires. NEMD analysis indicates that the broadened PDOS for amorphous contact renders superior overlap of phonon modes compared to their crystalline counterparts, leading to effective thermal coupling and high thermal conductance. Additionally, further measurements on the same nanowire at three different suspended lengths reveal suppressed thermal conductivity and a flattened temperature dependence compared to bulk Ge, due to enhanced phonon boundary scattering at the nanowire sample. These results provide important experimental evidence for the ultrahigh thermal conductance through the amorphous contact, offering valuable insights into thermal design for micro/nanoelectronic devices involving amorphous dielectric materials.

CRediT authorship contribution statement

Renzong Wang: Writing – original draft, Methodology, Investigation, Data curation. **Yucheng Xiong:** Writing – review & editing, Supervision, Project administration, Funding acquisition, Conceptualization. **Juekuan Yang:** Writing – review & editing, Methodology. **Zhichun Liu:** Validation, Methodology. **Shouhang Li:** Validation, Formal analysis. **Ge Chen:** Writing – review & editing, Supervision. **Ke Chen:** Formal analysis, Methodology, Validation. **Xiangjun Liu:** Writing – review & editing, Funding acquisition, Conceptualization.

Declaration of competing interest

The authors declare that they have no known competing financial interests or personal relationships that could have appeared to influence the work reported in this paper.

Data availability

Data will be made available on request.

Acknowledgements

This work was supported by the National Natural Science Foundation of China (Grant Nos. 52206080, 52150610495, and 12374027), Shanghai Pujiang Program (Grant No. 22PJ1400300), the Shanghai Municipal Natural Science Foundation (Grant No. 21TS1401500), and the Fundamental Research Funds for the Central Universities (Grant No. 2232022D-19).

Appendix B. Supplementary data

Supplementary data to this article can be found online at https://doi.org/10.1016/j.mtphys.2024.101469.

References

[1] M.J. Powell, The physics of amorphous-silicon thin-film transistors, IEEE Trans. Electron. Dev. 36 (1989) 2753–2763.
[2] J.S. Park, W.-J. Maeng, H.-S. Kim, J.-S. Park, Review of recent developments in amorphous oxide semiconductor thin-film transistor devices, Thin Solid Films 520 (2012) 1679–1693.
[3] T.H. Lee, D. Loke, K.J. Huang, W.J. Wang, S.R. Elliott, Tailoring transient-amorphous states: towards fast and power-efficient phase-change memory and neuromorphic computing, Adv. Mater. 26 (2014) 7493–7498.
[4] Y. Chen, B. Chen, L. Sun, W. Leng, Y. Meng, C. Gu, Y. Chen, T. Song, J. Huang, J. Wang, G. Wang, X. Shen, F. Rao, Nano-composite phase-change antimony thin film for fast and persistent memory operations, Mater. Today Phys. 22 (2022): 100584.
[5] Y. Lu, A. Alvarez, C.-H. Kao, J.-S. Bow, S.-Y. Chen, I.W. Chen, An electronic silicon-based memristor with a high switching uniformity, Nat. Electron. 2 (2019) 66–74.
[6] J. Zhang, F. Liu, D. Liu, Y. Yin, M. Wang, Z. Sa, L. Sun, X. Zheng, X. Zhuang, Z. Lv, W. Mu, Z. Jia, Y. Tan, F. Chen, Z.-X. Yang, Toward smart flexible self-powered near-UV photodetector of amorphous Ga_2O_3 nanosheet, Mater. Today Phys. 31 (2023): 100997.
[7] H. Wang, J. Ma, L. Cong, H. Zhou, P. Li, L. Fei, B. Li, H. Xu, Y. Liu, Piezoelectric effect enhanced flexible UV photodetector based on Ga_2O_3/ZnO heterojunction, Mater, Today Phys. 20 (2021): 100464.
[8] D.G. Cahill, P.V. Braun, G. Chen, D.R. Clarke, S. Fan, K.E. Goodson, P. Keblinski, W. P. King, G.D. Mahan, A. Majumdar, H.J. Maris, S.R. Phillpot, E. Pop, L. Shi, Nanoscale thermal transport. II. 2003–2012, Appl. Phys. Rev. 1 (2014): 011305.
[9] A. Giri, P.E. Hopkins, A review of experimental and computational advances in thermal boundary conductance and nanoscale thermal transport across solid interfaces, Adv. Funct. Mater. 30 (2020): 1903857.
[10] J. Chen, X. Xu, J. Zhou, B. Li, Interfacial thermal resistance: past, present, and future, Rev. Mod. Phys. 94 (2022): 025002.
[11] J. Zhou, H. Zhao, X. Fan, K. Yuan, Z. Wang, Z. Zhang, D. Li, X. Zhang, H. Chen, D. Tang, X. Zheng, J. Zhu, The effect of binding energy on optimizing the interfacial thermal transport in metal-MoS_2-dielectric nanostructures, Mater. Today Phys. 38 (2023): 101272.
[12] E. Elahi, M. Suleman, S. Nisar, P.R. Sharma, M.W. Iqbal, S.A. Patil, H. Kim, S. Abbas, V.D. Chavan, G. Dastgeer, J. Aziz, Robust approach towards wearable power efficient transistors with low subthreshold swing, Mater. Today Phys. 30 (2023): 100943.
[13] T. Kim, D. Kang, Y. Lee, S. Hong, H.G. Shin, H. Bae, Y. Yi, K. Kim, S. Im, 2D TMD channel transistors with ZnO nanowire gate for extended nonvolatile memory applications, Adv. Funct. Mater. 30 (2020): 2004140.
[14] S.R. Yadhuraj, B.V. Uma, S.G. Divakara, T.K. Subramanyam, S. Babu Gandla, Fabrication and study of amorphous silicon based MOS capacitor, Mater. Today Proc. 5 (2018) 21040–21046.
[15] H.S. Momose, T. Ohguro, K. Kojima, S. Nakamura, Y. Toyoshima, 1.5-nm gate oxide CMOS on [110] surface-oriented Si substrate, IEEE Trans. Electron. Dev. 50 (2003) 1001–1008.
[16] L. Yang, B. Latour, A.J. Minnich, Phonon transmission at crystalline-amorphous interfaces studied using mode-resolved atomistic Green's functions, Phys. Rev. B 97 (2018): 205306.
[17] W. Ih Choi, K. Kim, S. Narumanchi, Thermal conductance at atomically clean and disordered silicon/aluminum interfaces: a molecular dynamics simulation study, J. Appl. Phys. 112 (2012): 054305.
[18] Q. Wang, X. Wang, X. Liu, J. Zhang, Interfacial engineering for the enhancement of interfacial thermal conductance in GaN/AlN heterostructure, J. Appl. Phys. 129 (2021): 235102.
[19] A. Giri, P.E. Hopkins, J.G. Wessel, J.C. Duda, Kapitza resistance and the thermal conductivity of amorphous superlattices, J. Appl. Phys. 118 (2015): 165303.
[20] K. Gordiz, A. Henry, Phonon transport at interfaces between different phases of silicon and germanium, J. Appl. Phys. 121 (2017): 025102.
[21] A. Giri, S.W. King, W.A. Lanford, A.B. Mei, D. Merrill, L. Li, R. Oviedo, J. Richards, D.H. Olson, J.L. Braun, J.T. Gaskins, F. Deangelis, A. Henry, P.E. Hopkins, Interfacial defect vibrations enhance thermal transport in amorphous multilayers with ultrahigh thermal boundary conductance, Adv. Mater. 30 (2018): 1804097.
[22] S. Kwon, J. Zheng, M.C. Wingert, S. Cui, R. Chen, Unusually high and anisotropic thermal conductivity in amorphous silicon nanostructures, ACS Nano 11 (2017) 2470–2476.
[23] J.L. Braun, C.H. Baker, A. Giri, M. Elahi, K. Artyushkova, T.E. Beechem, P. M. Norris, Z.C. Leseman, J.T. Gaskins, P.E. Hopkins, Size effects on the thermal conductivity of amorphous silicon thin films, Phys. Rev. B 93 (2016): 140201.
[24] Y. Xiang, L. Cao, S. Conesa-Boj, S. Estrade, J. Arbiol, F. Peiro, M. Heiß, I. Zardo, J. R. Morante, M.L. Brongersma, A. Fontcuberta i Morral, Single crystalline and core–shell indium-catalyzed germanium nanowires—a systematic thermal CVD growth study, Nanotechnology 20 (2009): 245608.

[25] L. Shi, D. Li, C. Yu, W. Jang, D. Kim, Z. Yao, P. Kim, A. Majumdar, Measuring thermal and thermoelectric properties of one-dimensional nanostructures using a microfabricated device, J. Heat Tran. 125 (2003) 881–888.
[26] M.C. Wingert, Z.C. Chen, S. Kwon, J. Xiang, R. Chen, Ultra-sensitive thermal conductance measurement of one-dimensional nanostructures enhanced by differential bridge, Rev. Sci. Instrum. 83 (2012): 024901.
[27] S. Plimpton, Fast parallel algorithms for short-range molecular dynamics, J. Comput. Phys. 117 (1995) 1–19.
[28] K. Ding, H.C. Andersen, Molecular-dynamics simulation of amorphous germanium, Phys. Rev. B 34 (1986) 6987–6991.
[29] J. Tersoff, Modeling solid-state chemistry: interatomic potentials for multicomponent systems, Phys. Rev. B 39 (1989) 5566–5568.
[30] A.K. Rappe, C.J. Casewit, K.S. Colwell, W.A. Goddard, W.M. Skiff, UFF, a full periodic table force field for molecular mechanics and molecular dynamics simulations, J. Am. Chem. Soc. 114 (1992) 10024–10035.
[31] C. Yu, S. Saha, J. Zhou, L. Shi, A.M. Cassell, B.A. Cruden, Q. Ngo, J. Li, Thermal contact resistance and thermal conductivity of a carbon nanofiber, J. Heat Tran. 128 (2005) 234–239.
[32] H.W. Coleman, W.G. Steele, Experimentation, Validation, and Uncertainty Analysis for Engineers, Wiley, New York, 2018.
[33] K.L. Johnson, K. Kendall, a. Roberts, Surface energy and the contact of elastic solids, Pro. R Soc. Lond. Ser. A. Math. Phys. Sci. 324 (1971) 301–313.
[34] B.V. Derjaguin, V.M. Muller, Y.P. Toporov, Effect of contact deformations on the adhesion of particles, J. Colloid Interface Sci. 53 (1975) 314–326.
[35] D. Maugis, Adhesion of spheres: the JKR-DMT transition using a dugdale model, J. Colloid Interface Sci. 150 (1992) 243–269.
[36] J. Yang, M. Shen, Y. Yang, W.J. Evans, Z. Wei, W. Chen, A.A. Zinn, Y. Chen, R. Prasher, T.T. Xu, P. Keblinski, D. Li, Phonon transport through point contacts between graphitic nanomaterials, Phys. Rev. Lett. 112 (2014): 205901.
[37] E.T. Swartz, R.O. Pohl, Thermal boundary resistance, Rev. Mod. Phys. 61 (1989) 605–668.
[38] Z. Liang, P. Keblinski, Sound attenuation in amorphous silica at frequencies near the boson peak, Phys. Rev. B 93 (2016): 054205.
[39] L. Yang, Q. Zhang, Z. Cui, M. Gerboth, Y. Zhao, T.T. Xu, D.G. Walker, D. Li, Ballistic phonon penetration depth in amorphous silicon dioxide, Nano Lett. 17 (2017) 7218–7225.
[40] Y. Xiong, X. Yu, Y. Huang, J. Yang, L. Li, N. Yang, D. Xu, Ultralow thermal conductance of the van der Waals interface between organic nanoribbons, Mater. Today Phys. 11 (2019): 100139.
[41] M.T. Pettes, J. Maassen, I. Jo, M.S. Lundstrom, L. Shi, Effects of surface band bending and scattering on thermoelectric transport in suspended bismuth telluride nanoplates, Nano Lett. 13 (2013) 5316–5322.
[42] T. Tong, Y. Zhao, L. Delzeit, A. Kashani, M. Meyyappan, A. Majumdar, Height independent compressive modulus of vertically aligned carbon nanotube arrays, Nano Lett. 8 (2008) 511–515.
[43] B.N.J. Persson, M. Scaraggi, Theory of adhesion: role of surface roughness, J. Chem. Phys. 141 (2014): 124701.
[44] D.P. Schroeder, Z. Aksamija, A. Rath, P.M. Voyles, M.G. Lagally, M.A. Eriksson, Thermal resistance of transferred-silicon-nanomembrane interfaces, Phys. Rev. Lett. 115 (2015): 256101.
[45] H.-K. Lyeo, D.G. Cahill, Thermal conductance of interfaces between highly dissimilar materials, Phys. Rev. B 73 (2006): 144301.
[46] R.M. Costescu, M.A. Wall, D.G. Cahill, Thermal conductance of epitaxial interfaces, Phys. Rev. B 67 (2003): 054302.
[47] S.W. Fong, A. Sood, L. Chen, N. Kumari, M. Asheghi, K.E. Goodson, G.A. Gibson, H. S.P. Wong, Thermal conductivity measurement of amorphous dielectric multilayers for phase-change memory power reduction, J. Appl. Phys. 120 (2016): 015103.
[48] J.M. Dickey, A. Paskin, Computer simulation of the lattice dynamics of solids, Phys. Rev. 188 (1969) 1407–1418.
[49] M. Li, J. Zhang, X. Hu, Y. Yue, Thermal transport across graphene/SiC interface: effects of atomic bond and crystallinity of substrate, Appl. Phys. A 119 (2015) 415–424.
[50] D.G. Cahill, S.K. Watson, R.O. Pohl, Lower limit to the thermal conductivity of disordered crystals, Phys. Rev. B 46 (1992) 6131–6140.
[51] M. Asen-Palmer, K. Bartkowski, E. Gmelin, M. Cardona, A.P. Zhernov, A. V. Inyushkin, A. Taldenkov, V.I. Ozhogin, K.M. Itoh, E.E. Haller, Thermal conductivity of germanium crystals with different isotopic compositions, Phys. Rev. B 56 (1997) 9431–9447.
[52] M.C. Wingert, Z.C.Y. Chen, E. Dechaumphai, J. Moon, J.-H. Kim, J. Xiang, R. Chen, Thermal conductivity of Ge and Ge–Si core–shell nanowires in the phonon confinement regime, Nano Lett. 11 (2011) 5507–5513.
[53] J. Callaway, Model for lattice thermal conductivity at low temperatures, Phys. Rev. 113 (1959) 1046–1051.